Three in One: Three Different Molybdates Trapped in a Thiacalix[4]arene Protected Ag$_{72}$ Nanocluster for Structural Transformation and Photothermal Conversion

Zhi Wang, Yan-Jie Zhu, Olli Ahlstedt, Konstantinos Konstantinou, Jaakko Akola, Chen-Ho Tung, Fahri Alkan and Di Sun*

Dedication ((optional))

Abstract: Polyoxometalates (POMs) represent crucial intermediates in the formation of insoluble metal oxides from soluble metal ions, however, the rapid hydrolysis-condensation kinetics of Mo^{VI} or W^{VI} makes the direct characterization of coexisted molecular species in a given medium extremely difficult. Silver nanoclusters have shown versatile capacity to encapsulate diverse POMs, which provides an alternative scene to appreciate landscape of POMs in atomic precision. Here, we report a thiacalix[4]arene protected silver nanocluster (**Ag72b**) that simultaneously encapsulates three kinds of molybdates (MoO$_4^{2-}$, Mo$_6$O$_{22}^{8-}$ and Mo$_7$O$_{25}^{8-}$) *in situ* transformed from classic Lindqvist Mo$_6$O$_{19}^{2-}$, providing more deep understanding on the structural diversity and condensation growth route of POMs in solution. **Ag72b** is the first silver nanocluster trapping so many kinds of molybdates, which in turn exert collective template effect to aggregate silver atoms into a nanocluster. The post-reaction of **Ag72b** with AgOAc or PhCOOAg produces a discrete Ag$_{24}$ nanocluster (**Ag24a**) or an Ag$_{28}$ nanocluster based 1D chain structure (**Ag28a**), respectively. Moreover, the post-synthesized **Ag28a** can be utilized as potential ignition material for further application. This work not only provides an important model for unlocking dynamic features of POMs at atom-precise level but also pioneers a promising approach to synthesize silver nanoclusters from known to unknown.

Introduction

Noteworthy research on silver nanocluster has been ongoing in the emerging field of nanoscience owing to their structure diversities and attractive properties of catalysis, luminescence, chemical sensing and optical imaging.[1] Yet their synthetic chemistry is still an open-ended question involving the establishment of a universal synthesis method and structural modulation strategy. These circumstances

[*]   Z. Wang, Y.-J. Zhu, C-H Tung, Prof. D. Sun
        School of Chemistry and Chemical Engineering, State Key
        Laboratory of Crystal Materials, Shandong University, Ji'nan,
        250100, People's Republic of China
        E-mail: dsun@sdu.edu.cn
        O Ahlstedt, K Konstantinou, Prof. J. Akola
        Computational Physics Laboratory, Tampere University, FI-
        33014 Tampere, Finland.
        Prof. J. Akola
        Department of Physics, Norwegian University of Science and
        Technology, NO-7491 Trondheim, Norway.
        Prof. F. Alkan
        Department of Chemistry, Bilkent University, Ankara 06800,
        Turkey
        Supporting information for this article is available on the WWW
        under http://dx.doi.org/10.1002/anie.201xxxxxx.

have aroused great experimental efforts to push the progress for both synthesis protocol and structure identification of silver nanoclusters.[2] To date, an arsenal of silver nanoclusters has been gradually established and many members have been structurally determined at the atom-precise level.[3] Beyond the list of widely exploited ligands including thiolates, alkynyls, phosphines or/and their combination, the multidentate macrocycle oligomer of thiacalixarenes, i.e., *p-tert*-butylthiacalix[4]arene (H$_4$TC4A) and *p*-phenylthiacalix[4]arene (H$_4$PTC4A), with preorganized multiple coordination sites, becomes a more promising candidate in the construction of silver nanoclusters in terms of the improved structural rigidity, robustness and novelty.[4] The terminal phenoxyl groups and bridging sulfur atoms of these macrocycles can simultaneously hold "hard" and "soft" metal atoms, making them an ideal candidate for constructing silver nanoclusters. Liao and Hong groups have advanced the progress of metal-TC4A assemblies, especially in the construction of metal-organic polyhedra (MOP).[5] Some typical cases such as Co$_{32}$, Ni$_{40}$, and Mn$_{24}$ revealed that the shuttlecock-like {M$_4$(TC4A)} secondary building unit (SBU) is indispensable in their structures.[6] While scarce atomically precise TC4A^{4-} protected silver nanoclusters, such as Ag$_{18}$, Ag$_{34}$, Ag$_{35}$, Cl@Ag$_{42}$, (CrO$_4$)$_9$@Ag$_{88}$ as well as Ag$_{155}$, have been recently reported by Wang and Sun group,[7] no additional silver-TC4A nanoclusters have been characterized thus far. The difficulties of synthetic chemistry have limited the success in expanding the family of silver-TC4A nanoclusters and establishing the structure-function correlations.
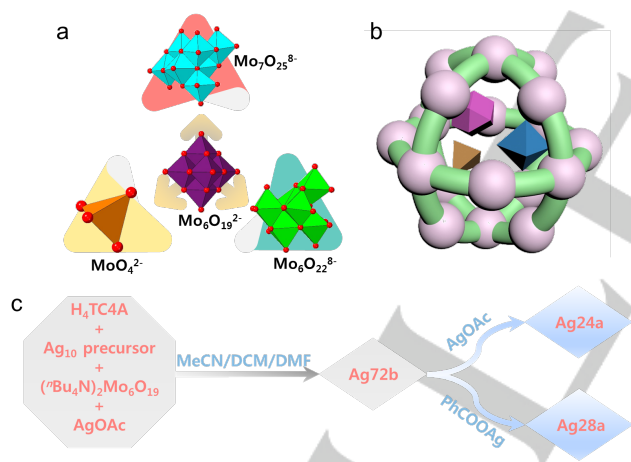
Although the enormous polyoxometallates (POMs) such as Keggin, Dawson and Lindqvist structures have been determined by single crystal X-ray diffraction (SCXRD), the atom-precise structures of kinetically controlled intermediate species remain a black box by virtue of their fast dynamic hydrolysis-condensation reaction in solution.[8] The molecular and electronic structures of metastable species of POMs are only substantiated by nuclear magnetic resonance, mass spectrum, small-angle X-ray scattering and other spectroscopy techniques.[8,9] Thanks to the adjustable compositions of POMs and their high negative charges with numerous bare oxygen coordination sites, POM-templated silver nanocluster chemistry has gained remarkable progresses.[10] Different sizes, charges, and geometries of POMs can lead to diverse silver shells, which in turn act as molecular containers to trap some active POM intermediates followed by structural determinations. So far, the POMs templated silver nanocluster of the highest nuclearity is

$[(W_5O_{19})(SO_4)]_2$@Ag$_{90}$, which only encapsulates two kinds of anion templates.[11] Encasing more than two kinds of POMs into one silver nanocluster can further grow our fundamental knowledge of the dynamic equilibrium of multiple POM species during their co-assembly process.

Despite the flourishment of anion templated silver nanoclusters, the reaction chemistry of them is still in its infancy.[12] Zang group reported a polyoxovanadate-templated Ag$_{30}$ nanocluster, which showed the reversible molecular symmetry transformation of inner $[V^V_{10}V^{IV}_2O_{34}]^{10-}$ from D_{3d} to C_{2h} under the external acid-base stimuli while keeping the silver shell intact.[13] Electrospray ionization mass spectrometry (ESI-MS) also demonstrated that TC4A^{4-} protected Ag$_{35}$ nanocluster can convert to Ag$_{34}$ and Ag$_{36}$ clusters with the assistance of HBF$_4$ and Et$_3$N.[7b] In 2018, Sun group has witnessed the structural transformation from [Mo$_6$O$_{22}$@Ag$_{44}$] to [Mo$_8$O$_{28}$@Ag$_{50}$] by reacting with PhCOOH and revealed a breakage-growth-reassembly (BGR) transformation mechanism under the guidance of time-dependent ESI-MS.[14] These sporadic discoveries indicated that the reaction chemistry of silver nanoclusters has the potential for making further breakthroughs in cluster synthetic chemistry and assembly mechanism, but remains enigmatic.

Scheme 1. (a) Three Different Molybdates *In Situ* Generated From Classic Lindqvist Mo$_6$O$_{19}$$^{2-}$. (b) Schematic Representation of a Silver Nanocluster Encapsulating Three Anions as Templates. (c) Synthesis Route for **Ag72b** and Its Post-Reaction with Silver Salts. Ag$_{10}$ precursor = {(HNEt$_3$)$_2$[Ag$_{10}$(^{t}BuPhS)$_{12}$]}$_n$

Within this context, our motivation is to gain fundamental understanding of the following: i) How many different POMs can be captured simultaneously in a POM-templated silver nanocluster; ii) what are the details of the electronic structure for the formed aggregate; iii) how does their synergistic template effect play out; and iv) what is the reaction chemistry of TC4A^{4-} protected silver nanocluster towards external stimuli. Herein, we report the synthesis, characterization, and electronic structure simulations of TC4A^{4-} and ^{t}BuPhS$^-$ (^{t}BuPhSH = 4-tert-butylbenzenethiol) co-protected silver nanocluster $[(Mo_7O_{25})(Mo_6O_{22})(MoO_4)$@Ag$_{72}$(TC4A)$_7$(^{t}BuPhS)$_{26}$(CH$_3$CN)$_9$(H$_2$O)]·11CH$_3$CN·CH$_2Cl_2$ (**Ag72b**) that traps three types of molybdates (Mo$_7$O$_{25}$$^{8-}$, Mo$_6O_{22}$$^{8-}$ and MoO$_4$$^{2-}$) together, which

are *in-situ* generated from the classic Lindqvist (^{n}Bu$_4$N)$_2$Mo$_6$O$_{19}$ (Scheme 1a). It is the first time that so many kinds of molybdates are wrapped inside one silver nanocluster (Scheme 1b). To our surprise, **Ag72b** as a raw material can respond to AgOAc or PhCOOAg to generate an Ag$_{24}$ nanocluster (**Ag24a**) or an Ag$_{28}$ nanocluster based 1D chain structure (**Ag28a**), respectively. Furthermore, these structures were fully characterized by SCXRD.[15] Such silver salt-stimulated nanocluster transformation is firstly demonstrated in POMs templated silver nanocluster protected by TC4A^{4-} ligand.

Results and Discussion

Ag72b was prepared by a typical recipe that involves stirring at room temperature followed by solvothermal method. Firstly, H$_4$TC4A, {(HNEt$_3$)$_2$[Ag$_{10}$(^{t}BuPhS)$_{12}$]}$_n$,[16] (^{n}Bu$_4$N)$_2$Mo$_6$O$_{19}$ and AgOAc were stirred in ternary mixed solvent of MeCN/DCM/DMF at room temperature to form a yellow turbid solution (Scheme 1c). Then the mixture was heated at 65 °C, and the yellowish-brown block crystals of **Ag72b** were crystallized in a yield of 11 % after cooling to room temperature (See in Supporting information). Keeping the experimental parameters consistent, the reproducibility is quite good. Moreover, **Ag72b** shows good reactivity toward external stimuli such as silver salts. When another portion of AgOAc or PhCOOAg was added into the reaction system for further solvothermal reaction after the crystals of **Ag72b** had appeared, another two new silver compounds were obtained as a discrete Ag$_{24}$ nanocluster (**Ag24a**) or an Ag$_{28}$ nanocluster based 1D coordination polymer (**Ag28a**), respectively. It is not possible to use the corresponding silver salt to directly synthesize **Ag24a** or **Ag28a**, suggesting that the post-reaction strategy can lead to some new silver nanoclusters that are otherwise not accessible by the traditional one-pot synthesis method. Despite the two-step process, the syntheses of **Ag24a** and **Ag28a** exhibited very good reproducibility.

SCXRD revealed that **Ag72b** crystallizes in triclinic space group $P\bar{1}$ (No. 2) and contains a complete cluster and lattice solvent guests of 11 CH$_3$CN and 1 CH$_2$Cl$_2$ in the asymmetric unit. As shown in Figure 1a and 1b, **Ag72b** consists of 72 silver atoms, three kinds of molybdates (1 Mo$_7$O$_{25}$$^{8-}$, 1 Mo$_6O_{22}$$^{8-}$ and 1 MoO$_4$$^{2-}$), two kinds of ligands (7 TC4A^{4-} and 26 ^{t}BuPhS$^-$) and two kinds of coordinated solvents (1 H$_2$O and 9 CH$_3$CN). Each unit cell contains two Ag$_{72}$ molecules (Figure S1). The local geometries around the Ag atoms are quite irregular and the coordination numbers vary from 2 to 6, finished by S, O, and N donors. The Ag···Ag contacts in **Ag72b** are in the range of 2.83-3.43 Å, indicating significant argentophilic interaction,[17] which consolidates the overall silver framework. We note that the three types of molybdates were not intentionally added to the reaction as they should be *in-situ* generated from (^{n}Bu$_4$N)$_2$Mo$_6$O$_{19}$. The MoO$_4$$^{2-}$ sitting at the equatorial region, together with inner two silver atoms (Ag5 and Ag46; Figure S2), divides **Ag72b** into two parts (**A** and **B** poles) and causes the silver shell to bulge from the equatorial region. Two poles of the silver framework are asymmetrically sustained by the inner Mo$_7$O$_{25}$$^{8-}$ (**A** pole) and

$Mo_6O_{22}^{8-}$ (**B** pole), respectively (Figure 1c). The **A** and **B** poles with 32 and 30 silver atoms sandwich the equatorial Ag_{33} annulus by sharing Ag_{12} and Ag_{11} metallamacrocycles up and down, respectively (green atoms in Figure 1c). The three molybdates are separately trapped under different silver framework regions, suggesting a size effect of template ions. In turn, the coordination of such a large amount of silver atoms to the oxygen atoms of molybdates suppresses the rapid amalgamation between these intermediate species, which facilitates the encapsulation of molybdates under the silver shells separately.
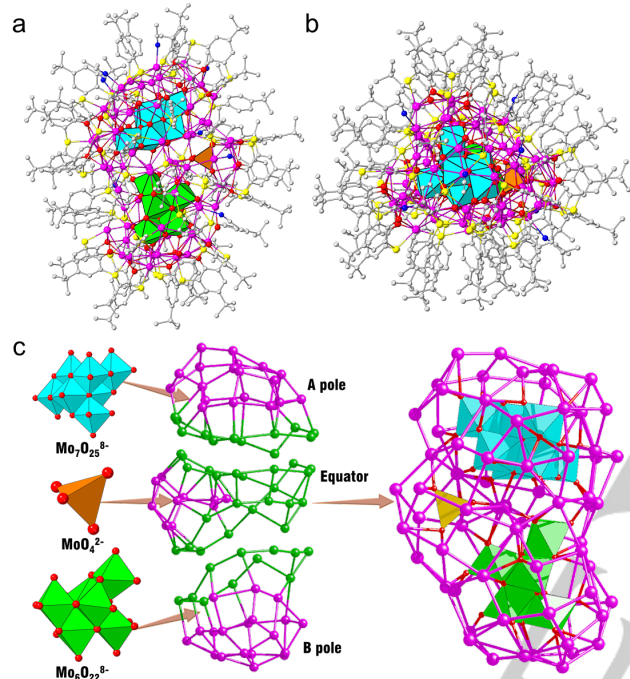
Figure 1. Side (a) and top view (b) of the total structure of **Ag72b**. All H atoms are removed for clarity. (c) The structural anatomy of the skeleton of **Ag72b**. All ligands are removed for clarity. Atom color labels: purple and green, Ag; yellow, S; gray, C; red, O; blue, N. Polyhedron color labels: MoO_6 octahedron in $Mo_6O_{22}^{8-}$ (green), $Mo_7O_{25}^{8-}$ (blue) and MoO_4^{2-} tetrahedron (orange).

The $Mo_6O_{22}^{8-}$ structure can be described as two MoO_6 octahedra anchored on a central Mo_4O_4 cube (Figure S3), or six edge-sharing MoO_6 octahedra. $Mo_6O_{22}^{8-}$ contains 8 bridging (4×μ_2, 2×μ_3, and 2×μ_4) and 14 terminal O atoms. This kind of $Mo_6O_{22}^{8-}$ unit has been observed in the previously reported $[(Mo_6O_{22})_2@Ag_{60}]$.[18] Total of 28 silver atoms cap on $Mo_6O_{22}^{8-}$ via partial bridging (4×μ_2, and 1×μ_3) and all terminal oxygen atoms (Figure S4). In comparison, $Mo_7O_{25}^{8-}$ has one more MoO_6 octahedron attached to the central Mo_4O_4 cube (Figure S5). This observation also indicates a possible growth mode from $Mo_6O_{22}^{8-}$ to $Mo_7O_{25}^{8-}$ in the solution by the attachment of a monomeric MoO_6 octahedron building block. The oxygen atoms in $Mo_7O_{25}^{8-}$ can be divided into 10 bridging (6×μ_2, 1×μ_3, and 3×μ_4) and 15 terminal atoms, in which all oxygen atoms coordinate with 28 silver atoms except for three inner μ_4 and two outer μ_2 oxygen atoms (Figure S6). Interestingly, $Mo_6O_{22}^{8-}$ and $Mo_7O_{25}^{8-}$ exhibit different geometries and nuclearities, however, both species coordinate with the same number of

silver atoms, which may be due to the presence of more μ_4 and μ_2 oxygen atoms in the latter (all of the μ_4 and 2 out of 6 μ_2 oxygen atoms are non-coordinated to any Ag). The Ag-O_{POMs} bond distances of **Ag72b** fall in the range of 2.14-2.8 Å. As a brand-new species of POMs, $Mo_7O_{25}^{8-}$ is not only firstly observed in anion-templated silver clusters but also in POMs chemistry. Amongst the previously reported POMs templated high-nuclearity silver nanoclusters,[19] such as $[(Mo_6O_{22})_2@Ag_{60}]$,[18] $[(EuW_{10}O_{36})_2@Ag_{72}]$, $[Mo_{20}O_{66}@Ag_{62}]$ and $[(PW_9O_{34})_2@Ag_{70}]$, the numbers of POMs embedded in one silver shell are no more than two and they are of the same type, except for $[(W_5O_{19})(SO_4)]_2@Ag_{90}$.[11] Therefore, encapsulating three kinds of molybdates in one Ag shell is so far unprecedented for the Ag nanocluster field.
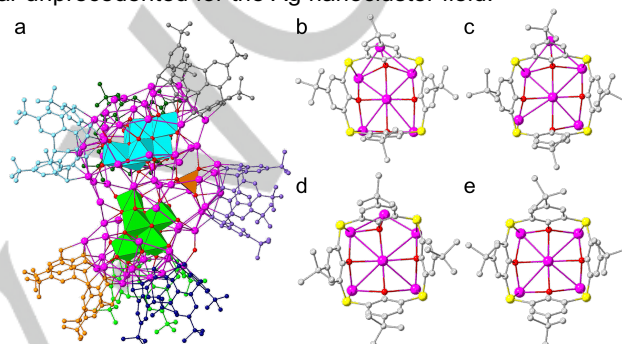

Figure 2. (a) The distribution of TC4A^{4-} (individually colored) on the surface of Ag_{72} shell; (b-e) The coordination modes of TC4A^{4-} observed in **Ag72b**. Color labels are the same to Figure 1.

There are three TC4A^{4-} ligands coordinated on each pole of **Ag72b**. The remaining one TC4A^{4-} covers the bulged area of the equator (Figure 2a). The seven TC4A^{4-} ligands adopt four coordination modes towards silver atoms (3×μ_6-κ_O^4:κ_O^3:κ_O^3:κ_O^3:κ_S^1:κ_S^1:κ_S^1:κ_S^1, 1×μ_6-κ_O^4:κ_O^3:κ_O^3:κ_O^2:κ_S^1:κ_S^1:κ_S^1:κ_S^1, 1×μ_6-κ_O^3:κ_O^3:κ_O^3:κ_O^3:κ_S^1:κ_S^1:κ_S^1:κ_S^1 and 2×μ_5-κ_O^3:κ_O^3:κ_O^3:κ_O^3:κ_S^1:κ_S^1:κ_S^1:κ_S^1) through phenoxyl groups and bridging sulfur atoms (Figure 2b-2e). Furthermore, since each hydroxyl group in TC4A^{4-} ligands is ligated to more than one silver atom, they should be completely deprotonated with Ag-O bond lengths falling in the range of 2.14-2.74 Å. Structure analysis indicated that {Ag_5(TC4A)} SBU plays a critical role in stabilizing the silver shell through the synergistic coordination effect of multiple sites. Since the long-axis of $Mo_7O_{25}^{8-}$ and $Mo_6O_{22}^{8-}$ in **Ag72b** are almost perpendicular to each other, **A** pole silver shell is much wider than **B** pole. Correspondingly, there are more exposed surface sites on the former than on the latter due to the bulkiness and rigidity of TC4A^{4-} ligands. To satisfy the saturated coverage of ligands on the silver shell, the partly exposed surface was filled by 26 *t*BuPhS$^-$ ligands and 9 coordinated MeCN molecules (Ag-S = 2.24 to 2.90 Å and Ag-N = 2.20-2.52 Å, Figure S7). Up to 9 CH_3CN molecules coordinate on the silver shell, which possibly endow **Ag72b** with a certain structural flexibility as observed in our previous case.[13]

Thanks to these weakly bonding sites and fairly good synthesis reproducibility, we could perform further studies on the reactivity of **Ag72b** with simple organic acid, base, or

silver salts. After all these attempts, it is worth mentioning that **Ag72b** can act as raw material to react with AgOAc or PhCOOAg (Scheme S1). Both the inner molybdates and outer silver shell cannot maintain their integrity in the reaction process which causes the isolation of two new silver compounds, a discrete Ag_{24} nanocluster (**Ag24a**) or an infinite 1D chain structure with Ag_{28} nanocluster as node (**Ag28a**).
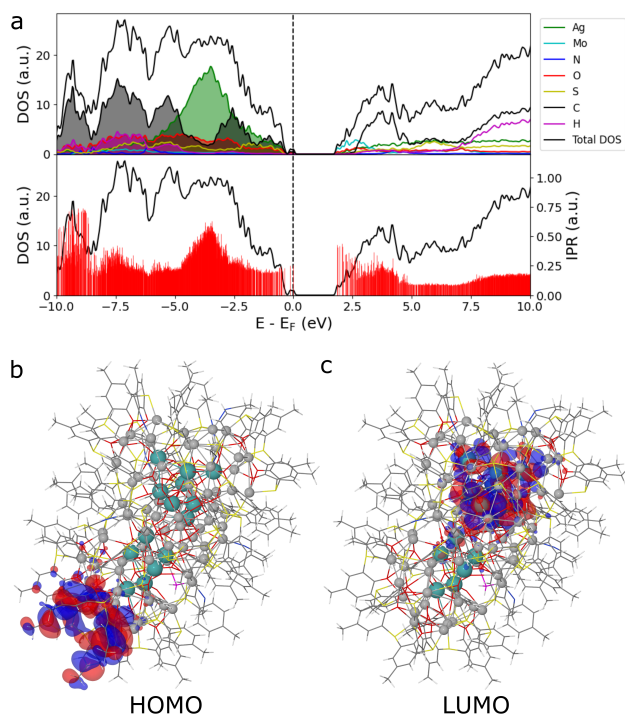

Figure 3. (a) Electronic density of states (DOS) with projections onto elements (top) and inverse participation ratios (IPR) in red that describe the degree of localization for individual orbitals (lower panel). (b-c) HOMO and LUMO orbitals showing increased weight on TC4A^{4-} and $Mo_7O_{25}^{8-}$, respectively. Mo (turquoise) and Ag (grey) atoms shown in ball-and-stick representation.

To investigate **Ag72b** theoretically, the crystal structure of the nanocluster was isolated, extremal tert-butyl groups of thiolates were replaced by methyl groups, and the missing hydrogens were added to the TC4A^{4-}/MePhS$^-$ side groups, 8 MeCN and one Ag-coordinating water molecule. The structure of 970 atoms was relaxed in the gas phase by using the density functional theory (DFT) and a hybrid PBE0 (Perdew–Burke–Erzenrhof) exchange-correlation functional. Some reorientations of ligands were observed in comparison with the crystal structure while the cluster core remained unchanged. The average Ag-Ag, Ag-Mo and Mo-Mo distances are 3.13±0.19 (3.15±0.17), 3.46±0.05 (3.47±0.07) and 3.30±0.05 (3.30±0.03) Å, respectively, with experimental values in parentheses. The Ag-O and Ag-S distances are 0-2% shorter than in the experimental structure, while the Mo-O distances have similar average values. The μ_2 oxygen of H_2O changes one of its Ag contacts to another which is reflected as a re-orientation of a nearby MeCN but this does not affect the electronic density of states (DOS, Figure 3a) at the Fermi level where the two highest occupied molecular

orbitals (HOMO) are associated with the TC4A^{4-} units capping $Mo_6O_{22}^{8-}$ (Figure 3b and Figure S8).

The DOS in Figure 3a shows that **Ag72b** has an electronic band gap of 1.84 eV. The DOS projections show more weight on Ag around the valence band edge, while Mo is predominant at the onset of the conduction band, as demonstrated for the lowest unoccupied molecular orbital (LUMO) in Figure 3c (see also Figure S9). The inverse participation ratios (IPR) display an increased weight at LUMO states associated with a more localized nature of the corresponding orbitals, and this is further verified by visualizations (Figure S8) which show accumulation around $Mo_7O_{25}^{8-}$ and the two other molybdates for LUMO+1 and LUMO+2. Previously, a similar analysis of a set of thiolate-protected Ag-S nanoclusters (without molybdates) showed a delocalization of LUMO orbitals within the whole nanocluster core in accordance with the superatom model.[20]

The effective charges (Bader method, Figure S10) show cationic charges for Ag (+0.60e) and Mo (+2.77e) which should not be confused with the nominal charges +1 and +4e, respectively. Sulfur and oxygen display two categories of charges depending on the local environment: -0.21 and -0.43e for S (TCA^{4-}/MePhS$^-$) and -0.57 and -1.05e for O (TCA^{4-}/molybdates). The net effective charges of individual TCA^{4-} and MePhS$^-$ groups are -2.62 and -0.36e, respectively, highlighting the electron-withdrawing effect of thiacalix[4]arenes. The charge transfer on H_2O and MeCN as well as extremal parts (Me/Ph) of thiolates is negligible.
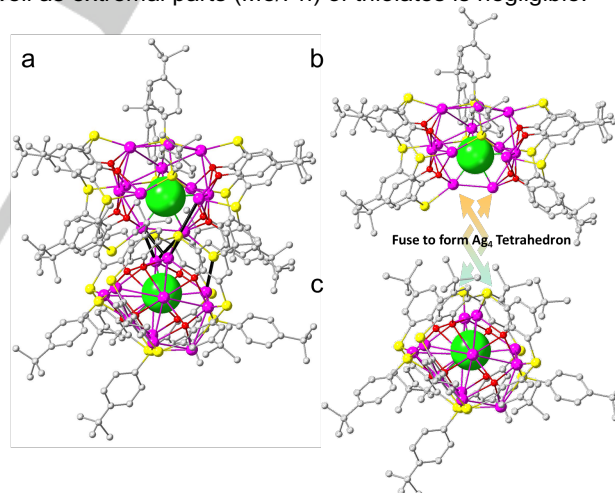

Figure 4. Total structure of **Ag24a** (a) formed by the fusion of two [Cl@Ag$_{12}$] units (b and c) with the help of Ag···Ag interactions and Ag-S bonds highlighted by black lines. Color labels: purple, Ag; yellow, S; gray, C; red, O; green, Cl, all H atoms and solvent molecules are not shown for clarity.

Both **Ag24a** and **Ag28a** crystallize in triclinic space group $P\bar{1}$ and include complete clusters and some solvent molecules in the asymmetric units. As revealed by crystallography, the composition of **Ag24a** and **Ag28a** are determined as [Cl$_2$@Ag$_{24}$(TC4A)$_4$(^{t}BuPhS)$_6$(DMF)$_3$]·3MeCN·2DMF (**Ag24a**) and {[Cl$_2$@Ag$_{32}$(TC4A)$_4$(^{t}BuPhS)$_8$(PhCOO)$_6$(MeCN)$_3$]·4MeCN}$_n$ (**Ag28a**). **Ag24a** can be roughly described as two

perpendicular [Cl@Ag$_{12}$] units (Figure 4a-4c) welded by Ag···Ag interactions and peripheral Ag-S bonds (black bond in Figure 4a). In other words, **Ag24a** is built from 2 Cl$^-$, 4 {Ag$_5$(TC4A)} SBUs, 4 ^{t}BuPhSAg units and 2 additional ^{t}BuPhS$^-$ ligands. Two Ag$_{24}$ molecules are present in one unit cell (Figure S11). Four {Ag$_5$(TC4A)} SBUs are connected to form an Ag$_4$ tetrahedron (Figure S12) with an average Ag···Ag distance of 2.86 Å. Two {Ag$_5$(TC4A)} SBUs in each [Cl@Ag$_{12}$] unit are bridged by two ^{t}BuPhSAg units and an additional ^{t}BuPhS$^-$ ligand. Two Cl$^-$ ions, as anion template, adopt μ$_4$ coordination mode to support the inner cavity underneath the silver shell. The Cl$^-$ ion may be originated from the C-Cl bond cleavage of dichloromethane.[21]
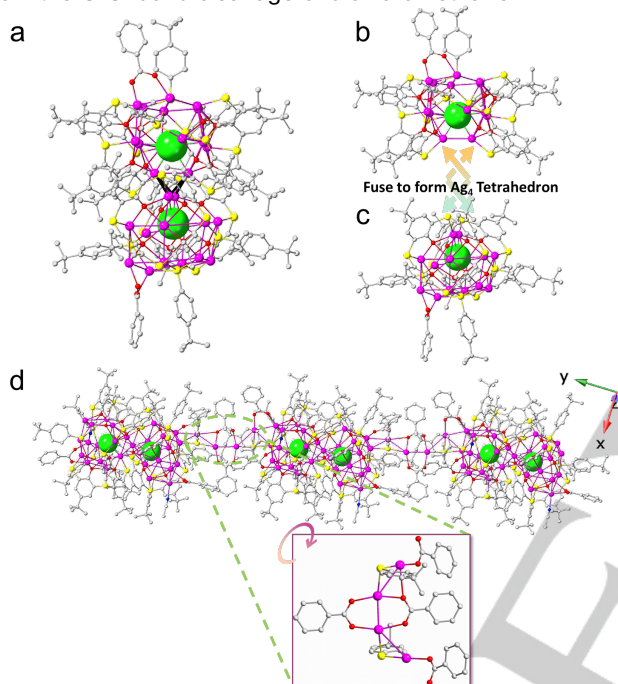

Figure 5. (a) The Ag$_{28}$ nanocluster unit in **Ag28a** formed by the fusion of two [Cl@Ag$_{14}$] units (b and c) with the help of Ag···Ag interactions highlighted by black lines. (d) The 1D chain structure of **Ag28a** built from Ag$_{28}$ nanocluster units extended by a bridge containing a [Ag$_2$(PhCOO)$_2$] and two [Ag(^{t}BuPhS)(PhCOO)] units. Silver atoms, PhCOO$^-$ and ^{t}BuPhS$^-$ ligands in the bridge are expanded in the inset. Color labels are same to Figure 4.

As shown in Figure 5a, the silver skeleton of **Ag28a** is similar to **Ag24a** but consists of two larger nearly orthogonal [Cl@Ag$_{14}$] units. In each [Cl@Ag$_{14}$] unit, two {Ag$_5$(TC4A)} SBUs are also welded by silver atoms and 3 ^{t}BuPhS$^-$ ligands. Two PhCOO$^-$ ligands adopt a μ$_2$-κ^1:κ^1 mode to cap on the top section of each [Cl@Ag$_{14}$] unit in **Ag28a**. Two [Cl@Ag$_{14}$] units in **Ag28a** are also connected to each other by forming a central Ag$_4$ tetrahedron with an average Ag···Ag separation of 2.81 Å, which is slightly shorter than that in **Ag24a** (Figure 5b and 5c). Two adjacent Ag$_{28}$ nanoclusters are further connected by a bridge consisting of a central binuclear [Ag$_2$(PhCOO)$_2$] and two [Ag(^{t}BuPhS)(PhCOO)] units at two sides of it, which produces a final Ag$_{28}$ nanocluster based 1D chain structure (Figure 5d). Note that the structure difference between **Ag24a** and **Ag28a** is mainly caused by the inducing effects of silver salts in the post-reaction. The {Ag$_5$(TC4A)}

SBUs in **Ag24a** and **Ag28a** are more distorted than those in **Ag72b**.
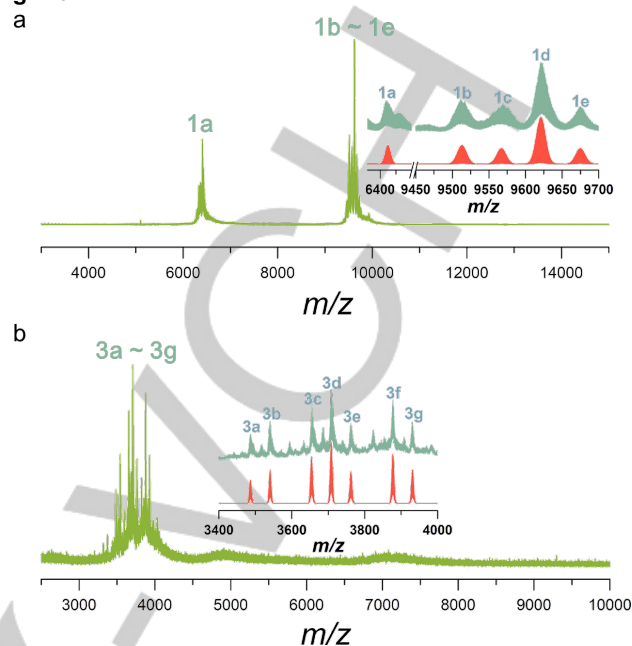

Figure 6. The positive-ion mode ESI-MS of **Ag72b** (a) and **Ag28a** (b). Inset: the magnified mass spectra of experimental (blue line) and simulated (red line) for each labeled species.

ESI-MS has been demonstrated to be a versatile method to examine the compositions, solution stabilities and the underlying assembly mechanism of nanoclusters.[22] The positive ion mode ESI-MS of **Ag72b** and **Ag28a** dissolved in CH$_2$Cl$_2$ and CH$_2$Cl$_2$/MeOH were recorded, respectively. There is a recognizable peak centered at *m/z* 6412.43 (**1a**) and a group of peaks (**1b**-**1e**) in the *m/z* range of 3000-15000 (Figure 6a). The charge states of **1a** and **1b-1e** determined by identifying the difference of isotope peaks are +3 and +2, respectively. The formula of **1a** can be assigned to [(Mo$_7$O$_{25}$)(Mo$_6$O$_{22}$)(MoO$_4$)@Ag$_{71}$(TC4A)$_7$(^{t}BuPhS)$_{26}$(H$_2$O)(CH$_2$Cl$_2$)]$^{3+}$ (calcd *m/z* 6412.35), which is formed by losing one Ag atom and a majority of solvation shell from **Ag72b**. The higher *m/z* region of ESI-MS contains the other four peaks in *m/z* 9000-15000, and the highest peak (**1d**) centered at 9621.13 is in agreement with the composition of [(Mo$_7$O$_{25}$)(Mo$_6$O$_{22}$)(MoO$_4$)@Ag$_{72}$(TC4A)$_7$(^{t}BuPhS)$_{26}$]$^{2+}$ (calcd *m/z* 9621.00). The *m/z* spacing between **1b** and **1c**, **1c** and **1d**, and **1d** and **1e** is 54, thus the actual mass difference is 54×2=108, corresponding to one Ag atom. Therefore, the formulae of **1b**, **1c** and **1e** were reasonably deduced from **1d** and summarized in the tabular form (Table S2). While the gradual loss of Ag atoms from the parent ion **1d** was detected under ESI-MS conditions, the presence of a high-abundance parent ion also implies the high solution stability of **Ag72b**. The loss of coordinated solvent molecules from the silver shell was also observed, providing further evidence for the flexibility of this cluster in solution.

As shown in Figure 6b, a group of +2 envelops are observed in the ESI-MS of **Ag28a** in *m/z* 2500-10000. After careful analysis and comparison of experimental and

simulated patterns, no parent ion was found for these peaks, while the most dominant peak centered on 3708.542 (**3d**) can be formulated as $[Cl_2@Ag_{32}(TC4A)_3(^tBuPhS)_3(PhCOO)_{10}(H_2O)_2]^{2+}$ (calcd m/z 3708.534). The envelops centered on 3486.921 (**3a**) and 3877.199 (**3f**) can be assigned to $[Cl_2@Ag_{25}(TC4A)_3(^tBuPhS)_7(PhCOO)_7(H_2O)(CH_3OH)]^{2+}$ (calcd m/z 3486.978) and $[Cl_2@Ag_{32}(TC4A)_3(^tBuPhS)_8(PhCOO)_6(CH_3OH)]^{2+}$ (calcd m/z 3877.163), respectively. The m/z spacing between **3a** and **3b**, **3c** and **3d**, **3d** and **3e**, and **3f** and **3g** is 54, corresponding to the mass of one Ag atom divided by +2. In accordance with this pattern, the remaining peaks can also be reasonably assigned and their respective formulae are detailed in Table S3. These results suggest that the 1D cluster-based chain is broken into several fragments with different silver nuclei ($Ag_{25\sim26}$ and $Ag_{31\sim33}$), and the ligand exchange between $^tBuPhS^-$ and $PhCOO^-$ also exists.
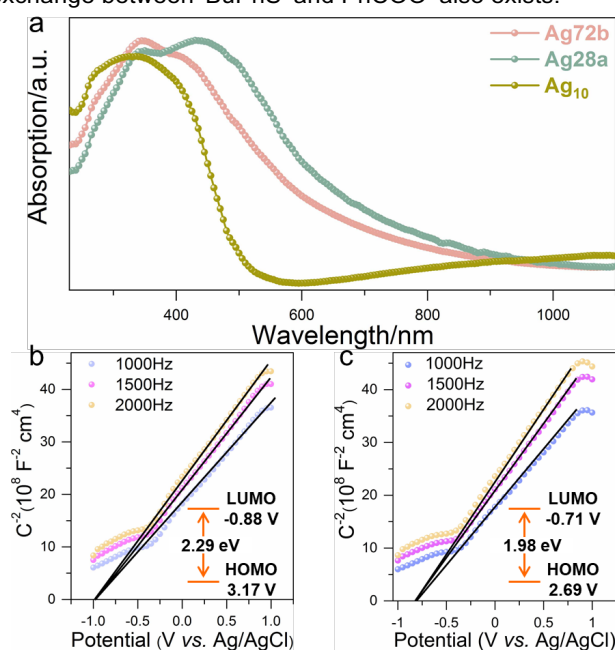

Figure 7. (a) The solid-state UV-Vis spectra of **Ag72b**, **Ag28a** and **Ag10**. Mott-Schottky (M-S) plots of **Ag72b** (b) and **Ag28a** (c). Ag10 precursor = $\{(HNEt_3)_2[Ag_{10}(^tBuPhS)_{12}]\}_n$.

The solid-state UV-Vis spectra of **Ag72b** and **Ag28a** were recorded at room temperature. Both display two humps in the wavelength range of 230-1100 nm (Figure 7a). They exhibit the same absorption peak centered 347 nm in the ultraviolet region which also was observed in the UV-Vis spectrum of $\{(HNEt_3)_2[Ag_{10}(^tBuPhS)_{12}]\}_n$, indicating the excited states of **Ag72b** and **Ag28a** are closely pertinent to the π-π^* transition of $^tBuPhS^-$ ligand. The visible absorption peaks, 411 nm for **Ag72b** and 439 nm for **Ag28a**, are tentatively assigned as ligand-to-metal charge transfer (LMCT, from S 3p to Ag 5s orbitals). The band gaps (E_g) of **Ag72b** and **Ag28a** were determined to be 2.29 and 1.98 eV respectively, (Figure S13) according to Kubelka-Munk function and Tauc plots, indicating their semiconductor characteristics.[23] Mott-Schottky (M-S) measurements of **Ag72b** and **Ag28a** were

also performed at the frequencies of 500, 1000 and 1500 Hz in darkness. As illustrated in Figure 7b and c, the positive slope of the linear plots indicated that both **Ag72b** and **Ag28a** are all n-type semiconductors.[24] The flat-band potentials (E_{fb}) of **Ag72b** and **Ag28a**, estimated from the extrapolation of M-S plots, are -0.98 V and -0.81 V versus Ag/AgCl, equivalent to -0.78 V and -0.61 V versus NHE, respectively. The conduction band potentials (E_{cb}), calculated by subtracting 0.1 V from E_{fb} value, are -0.88 V and -0.71 V, corresponding to LUMO of **Ag72b** and **Ag28a** respectively. Combined with the E_g determined from UV-Vis spectra, the valence band (HOMO) are calculated to be 3.17 V (**Ag72b**) and 2.69 V (**Ag28a**).

Taking into account that the calculated electronic band gap in DFT does not necessarily correspond to the optical one, a delta self-consistent field (ΔSCF) approximation was applied by exciting **Ag72b** to a triplet spin-state and calculating the total energy difference. The obtained value of 2.20 eV is in good agreement with the extrapolated experimental value of 2.29 eV. An optical absorption spectrum calculation (Figure S14) was also performed up to 3.6 eV and it shows a monotonic increase from the threshold above 2.0 eV in a qualitative agreement with the experimental profile. The obtained oscillator strengths for individual transitions show small values within the threshold region (across the band gap), $i.e.$ the first transitions from the HOMO orbitals associated with $TC4A^{4-}$ to the molybdate-localized LUMO orbitals (Figure 3b-c) are weak.

Both **Ag72b** and **Ag28a** emit silent at room and cryogenic temperatures under 450 nm wavelength irradiation, suggesting a very weak radiative transition, with nonradiative migration becoming the predominant mechanism for energy release. Such nonradiative migrations can trigger photothermal conversion, which promotes **Ag72b** and **Ag28a** as the photothermal materials.[7a, 7f, 25] Here, precise temperature measurements were recorded for **Ag72b** and **Ag28a** with various concentrations under 450 nm laser irradiation (0.5 W cm^{-2}) at a distance of 15 cm and plotted in Figure 8. No obvious temperature rise (< 1 ^{o}C) was detected for the blank TCM solution. The temperature of **Ag72b** solution (50 μM in TCM solution) was elevated from 24 to 31 ^{o}C in 240 s, suggesting it has the light-to-heat conversion ability (Figure 8a and 8c). The plateau temperature increased significantly with the increase in concentration, as it reached 42.3 ^{o}C at a concentration of 200 μM. In contrast, **Ag28a** achieved a maximum temperature of about 52.3 ^{o}C in a concentration of 200 μM (Figure 8b and 8c). At each time point, the temperature of **Ag28a** was higher than **Ag72b** with the same concentration, indicative of the faster heating capability of **Ag28a**. The difference between the photothermal effect of **Ag72b** and **Ag28a** stems from the difference in their absorption properties (Figure S15). The photothermal conversion efficiency (Figure S16 and S17) of **Ag72b** was calculated to be 46.93 %, which is lower than that of **Ag28a** (49.93 %). The photothermal stability was also investigated by reversibly irradiating and naturally cooling the TCM solutions of **Ag72b** and **Ag28a** with and without 450 nm laser (Figure 8d and S18). Their maximum temperatures remains nearly unchanged for at least 6 cycles, suggesting

their high photothermal stabilities. As its enhanced light-absorption intensity at the same concentration compared to **Ag72b**, **Ag28a** exhibits superior photothermal performance over **Ag72b**.

The photothermal performance of **Ag72b** and **Ag28a** in the solid state was also investigated under 450 nm laser irradiation at a distance of 15 cm. As depicted in Figure 8e and 8f, the plateau temperature of **Ag72b** and **Ag28a** can be elevated to 56 °C in 3.6 s and 142 °C in 4.7 s, respectively, with a power density of 0.3 W cm^{-2}. As the laser power continues to increase, so do the plateau temperatures. However, the maximum temperature of **Ag72b** (149 °C) is still lower than that of **Ag28a** (257 °C) at the power density of 0.5 W cm^{-2}. This result reveals that **Ag28a** shows superior photothermal conversion than **Ag72b** either in the solution or solid-state, which promoted us to investigate whether they can act as remote ignition material. The ignition material is important as it can initiate a fire and play a pivotal role in fire growth.[26] Here we used the sample of **Ag72b** and **Ag28a** coated match (denoted as **Ag72b/match** and **Ag28a/match**) as the object of study, respectively (Figure S19). If the remote ignition experiment is successful, we can realize the controllability and safety of the ignition process. As shown in Figure 8g, the match can only be ignited with power densities

larger than 0.3 W cm^{-2} with a 450 nm laser at a distance of 15 cm. The **Ag72b/match** can also only be ignited at the same conditions, but the ignition time can be reduced from 20.3 s to 12.6 s with the **Ag72b/match**. Furthermore, the ignition time further shortens to 7.0 s when the power density is increased to 0.5 W cm^{-2}. In comparison, the **Ag28a/match** can be ignited with a power density of 0.2 W cm^{-2} with an ignition time of 24.8 s. When the power density is increased to 0.5 W cm^{-2}, the ignition time can be reduced to 4.8 s. Considering the remote ignition properties, the distance between the laser and the sample emerges as a critical factor influencing the merit of the remote ignition materials. When the laser power density was fixed to 0.5 W cm^{-2}, all the samples including the match could be ignited within a range of 10 to 25 cm (Figure 8h). The variation in ignition time becomes more apparent when analyzing the impact of reduced distances between 25 and 10 cm. The ignition time of the **match**, **Ag72b/match**, and **Ag28a/match** decreases from 17.2, 12.4, and 10.6 s to 7.2, 5.0, and 2.8 s respectively. These results show that the photothermal performance of the samples follows the trend of **Ag28a/match** > **Ag72b/match** > **match**, and **Ag28a/match** can be used as a potential ignition material as it can provide a shorter ignition time with the lower power density and longer distance.
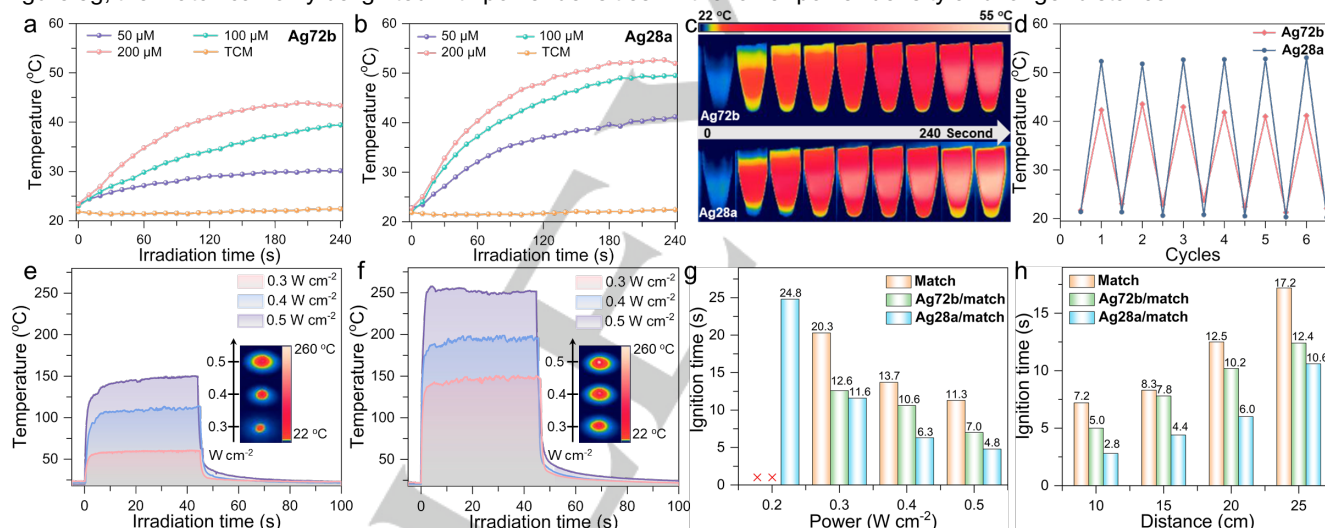

Figure 8. Photothermal conversion curves of **Ag72b** (a) and **Ag28a** (b) at different concentrations under 450 nm laser irradiation (0.5 W cm^{-2}). (c) Thermal images of **Ag72b** and **Ag28a** at a concentration of 200 μM. (d) Stability study of **Ag72b** and **Ag28a** under the photothermal heating and cooling cycles. The laser irradiation wavelength was at 450 nm with a power density of 0.5 W cm^{-2}. Photothermal conversion curves of **Ag72b** (e) and **Ag28a** (f) in the solid state under 450 nm laser irradiation (0.3, 0.4, and 0.5 W cm^{-2}). Insets: the thermal images of **Ag72b** and **Ag28a** at highest temperature with different laser power densities. The comparison of the ignition time of **match**, **Ag72b/match** and **Ag28a/match** at different power densities (g) and distances (h).

CONCLUSIONS

In summary, three kinds of molybdates (Mo$_7$O$_{25}^{8-}$, Mo$_6$O$_{22}^{8-}$ and MoO$_4^{2-}$) *in situ* generated from the classic Lindqvist Mo$_6$O$_{19}^{2-}$ were encapsulated in a novel 72-nuclei silver nanocluster (**Ag72b**) co-protected by TC4A^{4-} and ^{t}BuPhS$^-$ for the first time. The successful characterization of this silver nanocluster provides the first model to accurately recognize the coexisting multiple forms of molybdate species in solution, which in turn helps us to establish the correlation of three molybdates and propose possible formation

mechanism. Moreover, **Ag72b** can further react with silver salts (AgOAc or PhCOOAg) to produce two new silver compounds, a discrete Ag$_{24}$ nanocluster (**Ag24a**) and an infinite 1D chain structure with the Ag$_{28}$ nanocluster as node (**Ag28a**). The photothermal conversion performance of the post-synthesized **Ag28a** was superior to **Ag72b** and can be used as the potential ignition material. This work not only provides a shortcut for the syntheses of novel silver nanoclusters but also furnishes direct evidence for understanding the solution species diversity of molybdates and their correlation in a black box.

Acknowledgements

[1] a) R. Jin, C. Zeng, M. Zhou, Y. Chen, *Chem. Rev.* **2016**, *116*, 10346-10413; b) S. Sharma, K. K. Chakrahari, J.-Y. Saillard, C. W. Liu, *Acc Chem Res* **2018**, *51*, 2475-2483; c) S. Wang, Q. Li, X. Kang, M. Zhu, *Acc Chem Res* **2018**, *51*, 2784-2792; d) Y. Du, H. Sheng, D. Astruc, M. Zhu, *Chem. Rev.* **2020**, *120*, 526-622; e) O. Veselska, A. Demessence, *Coord Chem Rev* **2018**, *355*, 240-270.

[2] a) S. Bestgen, O. Fuhr, B. Breitung, V. S. K. Chakravadhanula, G. Guthausen, F. Hennrich, W. Yu, M. M. Kappes, P. W. Roesky, D. Fenske, *Chem Sci* **2017**, *8*, 2235-2240; b) Z. Wang, R. K. Gupta, G.-G. Luo, D. Sun, *Chem Rec* **2020,** *20*, 389-402; c) J. Yan, B. K. Teo, N. Zheng, *Acc Chem Res* **2018**, *51*, 3084-3093.

[3] a) O. Fuhr, S. Dehnen, D. Fenske, *Chem Soc Rev* **2013**, *42*, 1871-1906; b) I. Chakraborty, T. Pradeep, *Chem. Rev.* **2017**, *117*, 8208-8271; c) Q.-M. Wang, Y.-M. Lin, K.-G. Liu, *Acc Chem Res* **2015**, *48*, 1570-1579; d) Y.-P. Xie, J.-L. Jin, G.-X. Duan, X. Lu, T. C. W. Mak, *Coord Chem Rev* **2017**, *331*, 54-72; e) B. Li, H.-T. Fan, S.-Q. Zang, H.-Y. Li, L.-Y. Wang, *Coord Chem Rev* **2018**, *377*, 307-329; f) X. Kang, M. Zhu, *Coord Chem Rev* **2019**, *394*, 1-38.

[4] a) M. Diecke, C. Schrenk, A. Schnepf, *Angew Chem Int Ed* **2020**, *59*, 14418-14422; b) Y.-T. Chen, I. S. Krytchankou, A. J. Karttunen, E. V. Grachova, S. P. Tunik, P.-T. Chou, I. O. Koshevoy, *Organometallics* **2017**, *36*, 480-489; c) H. Shen, K. Kubo, S. Kume, L. Zhang, T. Mizuta, *Dalton Trans* **2017**, *46*, 16199-16204; d) A. K. Gupta, A. Orthaber, *Chem-Eur J* **2018**, *24*, 7536-7539; e) Y. Liu, B. K. Najafabadi, M. A. Fard, J. F. Corrigan, *Angew Chem Int Ed* **2015**, *54*, 4832-4835; f) M. Qu, H. Li, L.-H. Xie, S.-T. Yan, J.-R. Li, J.-H. Wang, C.-Y. Wei, Y.-W. Wu, X.-M. Zhang, *J Am Chem Soc* **2017**, *139*, 12346-12349; g) R. Kumar, Y. O. Lee, V. Bhalla, M. Kumar, J. S. Kim, *Chem Soc Rev* **2014**, *43*, 4824-4870; h) Y. Bi, S. Du, W. Liao, *Coord Chem Rev* **2014**, *276*, 61-72.

[5] a) M. Liu, W. Liao, C. Hu, S. Du, H. Zhang, *Angew Chem Int Ed* **2012**, *51*, 1585-1588; b) Y. Bi, G. Xu, W. Liao, S. Du, X. Wang, R. Deng, H. Zhang, S. Gao, *Chem. Commun.* **2010**, *46*, 6362-6364; c) K. Xiong, F. Jiang, Y. Gai, Y. Zhou, D. Yuan, K. Su, X. Wang, M. Hong, *Inorg Chem* **2012**, *51*, 3283-3288; d) K. Xiong, X. Wang, F. Jiang, Y. Gai, W. Xu, K. Su, X. Li, D. Yuan, M. Hong, *Chem. Commun.* **2012**, *48*, 7456-7458.

[6] a) Y. Bi, X.-T. Wang, W. Liao, X. Wang, X. Wang, H. Zhang, S. Gao, *J Am Chem Soc* **2009**, *131*, 11650-11651; b) X. Hang, B. Liu, X. Zhu, S. Wang, H. Han, W. Liao, Y. Liu, C. Hu, *J Am Chem Soc* **2016**, *138*, 2969-2972; c) K.-C. Xiong, F.-L. Jiang, Y.-L. Gai, D.-Q. Yuan, D. Han, J. Ma, S.-Q. Zhang, M.-C. Hong, *Chem-Eur J* **2012**, *18*, 5536-5540.

[7] a) Z. Wang, L. Li, L. Feng, Z.-Y. Gao, C.-H. Tung, L.-S. Zheng, D. Sun, *Angew Chem Int Ed* **2022**, *61*, e202200823; b) Z.-J. Guan, F. Hu, S.-F. Yuan, Z.-A. Nan, Y.-M. Lin, Q.-M. Wang, *Chem Sci* **2019**, *10*, 3360-3365; c) Z.-J. Guan, J.-L. Zeng, Z.-A. Nan, X.-K. Wan, Y.-M. Lin, Q.-M. Wang, *Sci Adv* **2016**, *2*, e1600323; d) Z. Wang, H.-F. Su, L.-P. Zhang, J.-M. Dou, C.-H. Tung, D. Sun, L. Zheng, *ACS Nano* **2022**, *16*, 4500-4507; e) Z. Wang, H.-F. Su, Y.-W. Gong, Q.-P. Qu, Y.-F. Bi, C.-H. Tung, D. Sun, L.-S. Zheng, *Nat Commun* **2020**, *11*, 308; f) Z. Wang, F. Alkan, C. M. Aikens, M. Kurmoo, Z.-Y. Zhang, K.-P. Song, C.-H. Tung, D. Sun, *Angew Chem Int Ed* **2022**, *61*, e202206742.

[8] J. J. Borrás-Almenar, E. Coronado, A. Müller, M. Pope, *Polyoxometalate molecular science,* Springer Science & Business Media, **2003**.

[9] W. Wang, M. Amiri, T. Huang, L. N. Zakharov, Y. Zhang, M. Nyman, *Inorg Chem* **2019**, *58*, 5555-5560.

[10] a) G.-X. Duan, Y.-P. Xie, J.-L. Jin, L.-P. Bao, X. Lu, T. C. W. Mak, *Chem-Eur J* **2018**, *24*, 6762-6768; b) Y.-P. Xie, T. C. W. Mak, *J Clust Sci* **2014**, *25*, 189-204; c) G.-G. Gao, P.-S. Cheng, T. C. W. Mak, *J Am Chem Soc* **2009**, *131*, 18257-18259.

[11] J.-W. Liu, H.-F. Su, Z. Wang, Y.-A. Li, Q.-Q. Zhao, X.-P. Wang, C.-H. Tung, D. Sun, L.-S. Zheng, *Chem. Commun.* **2018**, *54*, 4461-4464.

[12] a) B.-J. Yan, X.-S. Du, R.-W. Huang, J.-S. Yang, Z.-Y. Wang, S.-Q. Zang, T. C. W. Mak, *Inorg. Chem.* **2018**, *57*, 4828-4832; b) Z. Wang, H.-F. Su, M. Kurmoo, C.-H. Tung, D. Sun, L.-S. Zheng, *Nat Commun* **2018**, *9*, 2094; c) J.-W. Liu, L. Feng, H.-F. Su, Z. Wang, Q.-Q. Zhao, X.-P. Wang, C.-H. Tung, D. Sun, L.-S. Zheng, *J Am Chem Soc* **2018**, *140*, 1600-1603.

[13] H. Liu, C.-Y. Song, R.-W. Huang, Y. Zhang, H. Xu, M.-J. Li, S.-Q. Zang, G.-G. Gao, *Angew Chem Int Ed* **2016**, *55*, 3699-3703.

[14] Z. Wang, H.-F. Su, C.-H. Tung, D. Sun, L.-S. Zheng, *Nat Commun* **2018**, *9*, 4407.

[15] CCDC deposition numbers 2295962 (**Ag72b**), 2295963 (**Ag24a**), 2295964 (**Ag28a**) contain the supplementary crystallographic data for this article. These data can be obtained free of charge by the joint Cambridge Crystallographic Data Centre and Fachinformationszentrum Karlsruhe Access Structures service.

[16] K. L. Tang, X. J. Xie, L. Zhao, Y. H. Zhang, X. L. Jin, *Eur J Inorg Chem* **2004**, 78-85.

[17] a) H. Schmidbaur, A. Schier, *Angew Chem Int Ed* **2015**, *54*, 746-784; b) H. Wu, X. He, B. Yang, C.-C. Li, L. Zhao, *Angew Chem Int Ed* **2021**, *60*, 1535-1539; c) X. Liu, J. Chen, J. Yuan, Y. Li, J. Li, S. Zhou, C. Yao, L. Liao, S. Zhuang, Y. Zhao, H. Deng, J. Yang, Z. Wu, *Angew Chem Int Ed* **2018**, *57*, 11273-11277; d) Z. Wang, J.-W. Liu, H.-F. Su, Q.-Q. Zhao, M. Kurmoo, X.-P. Wang, C.-H. Tung, D. Sun, L.-S. Zheng, *J Am Chem Soc* **2019**, *141*, 17884-17890; e) J.-Y. Liu, F. Alkan, Z. Wang, Z.-Y. Zhang, M. Kurmoo, Z. Yan, Q.-Q. Zhao, C. M. Aikens, C.-H. Tung, D. Sun, *Angew Chem Int Ed* **2019**, *58*, 195-199; f) Z. Wang, Y.-M. Sun, Q.-P. Qu, Y.-X. Liang, X.-P. Wang, Q.-Y. Liu, M. Kurmoo, H.-F. Su, C.-H. Tung, D. Sun, *Nanoscale* **2019**, *11*, 10927-10931.

[18] J. Qiao, K. Shi, Q.-M. Wang, *Angew Chem Int Ed* **2010**, *49*, 1765-1767.

[19] a) S.-S. Zhang, H.-F. Su, Z. Wang, X.-P. Wang, W.-X. Chen, Q.-Q. Zhao, C.-H. Tung, D. Sun, L.-S. Zheng, *Chem-Eur J* **2018**, *24*, 1998-2003; b) R.-W. Huang, Q.-Q. Xu, H.-L. Lu, X.-K. Guo, S.-Q. Zang, G.-G. Gao, M.-S. Tang, T. C. W. Mak, *Nanoscale* **2015**, *7*, 7151-7154; c) Z.-G. Jiang, K. Shi, Y.-M. Lin, Q.-M. Wang, *Chem. Commun.* **2014**, *50*, 2353-2355.

[20] a) J.-Q. Goh, S. Malola, H. Hakkinen, J. Akola, *J. Phys. Chem. C* **2015**, *119*, 1583-1590; b) J. Q. Goh, J. Akola, *J. Phys. Chem. C* **2015**, *119*, 21165-21172.

[21] a) F. Hu, J.-J. Li, Z.-J. Guan, S.-F. Yuan, Q.-M. Wang, *Angew Chem Int Ed* **2020**, *59*, 5312-5315; b) A. Ghosh, R.-W. Huang, B. Alamer, E. Abou-Hamad, M. N. Hedhili, O. F. Mohammed, O. M. Bakr, *ACS Materials Lett.* **2019**, *1*, 297-302.

[22] a) Q. Yao, T. Chen, X. Yuan, J. Xie, *Acc Chem Res* **2018**, *51*, 1338-1348; b) Z. Wang, H.-F. Su, Y.-Z. Tan, S. Schein, S.-C. Lin, W. Liu, S.-A. Wang, W.-G. Wang, C.-H. Tung, D. Sun, L.-S. Zheng, *Proc. Natl. Acad. Sci. U.S.A.* **2017**, *114*, 12132-12137; c) Y.-K. Deng, H.-F. Su, J.-H. Xu, W.-G. Wang, M. Kurmoo, S.-C. Lin, Y.-Z. Tan, J. Jia, D. Sun, L.-S. Zheng, *J Am Chem Soc* **2016**, *138*, 1328-1334; d) E. Khatun, M. Bodiuzzaman, K. S. Sugi, P. Chakraborty, G. Paramasivam, W. A. Dar, T. Ahuja, S. Antharjanam, T. Pradeep, *ACS Nano* **2019**, *13*, 5753-5759; e) U. Warzok, L. K. Mahnke, W. Bensch, *Chem-Eur J* **2019**, *25*, 1405-1419; f) W. Xuan, R. Pow, N. Watfa, Q. Zheng, A. J. Surman, D.-L. Long, L. Cronin, *J Am Chem Soc* **2019**, *141*, 1242-1250.

[23] N. K. Chaki, S. Mandal, A. C. Reber, M. Qian, H. M. Saavedra, P. S. Weiss, S. N. Khanna, A. Sen, *ACS Nano* **2010**, *4*, 5813-5818.

[24] a) S. Saha, G. Das, J. Thote, R. Banerjee, *J Am Chem Soc* **2014**, *136*, 14845-14851; b) X. Hu, M. Han, L. Shao, C. Zhang, L. Zhang, S. P. Kelley, C. Zhang, J. Lin, S. J. Dalgarno, D. A. Atwood, S. Feng, J. L. Atwood, *Angew Chem Int Ed* **2021**, *60*, 10516-10520.

[25] a) L. Zhao, Y. Liu, R. Xing, X. Yan, *Angew Chem Int Ed* **2020**, *59*, 3793-3801; b) Z. Wang, Y.-J. Zhu, B.-L. Han, Y.-Z. Li, C.-H. Tung, D. Sun, *Nat*

Commun **2023**, *14*, 5295; c) K. Sheng, Z. Wang, L. Li, Z.-Y. Gao, C.-H. Tung, D. Sun, *J Am Chem Soc* **2023**, *145*, 10595-10603.

[26] A. Atreya, *Philos T R Soc A* **1998**, *356*, 2787-2813.

Entry for the Table of Contents

RESEARCH ARTICLE

Three different molybdates were trapped simultaneously in a thiacalix[4]arene-protected Ag_{72} nanocluster (**Ag72b**). The reaction of **Ag72b** with AgOAc resulted in the formation of a discrete Ag_{24} nanocluster (**Ag24a**), whereas reaction with PhCOOAg gave a Ag_{28} nanocluster-based 1D chain structure (**Ag28a**). Photothermal conversion performance demonstrated that the **Ag28a** is superior to the **Ag72b**.
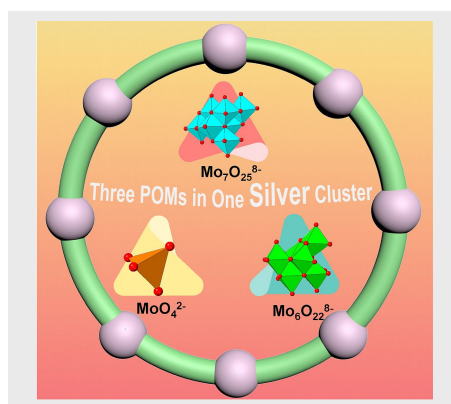
Three POMs in One Silver Cluster

$Mo_7O_{25}^{8-}$

MoO_4^{2-}

$Mo_6O_{22}^{8-}$

Zhi Wang, Yan-Jie Zhu, Olli Ahlstedt, Konstantinos Konstantinou, Jaakko Akola, Chen-Ho Tung, Fahri Alkan and Di Sun*

Page No. – Page No.

Three in One: Three Different Molybdates Trapped in a Thiacalix[4]arene Protected Ag_{72} Nanocluster for Structural Transformation and Photothermal Conversion